

# Angle-Time-Energy Images of Ultra-High Energy Cosmic Ray Sources

Günter Sigl\*

*\*Department of Astronomy & Astrophysics  
Enrico Fermi Institute, The University of Chicago, Chicago, IL 60637-1433*

**Abstract.** Substantial amount of information both on the source and on characteristics of intercepting magnetic fields is encoded in the distribution in arrival times, directions, and energies of charged ultra-high energy cosmic rays from discrete sources. We present a numerical approach that allows to extract such information from data from next generation experiments.

## INTRODUCTION

The origin of ultra-high energy cosmic rays is still a major unresolved mystery in astrophysics. It is hard to imagine a mechanism producing particles of energy up to several 100 EeV ( $= 10^{20}$  eV). In addition, sources must be closer than  $\simeq 50$  Mpc because of the limited range of nucleons due to photo-pion production at these energies. No obvious astrophysical sources have been found within this distance [1,2]. Although deflection of charged primaries can be strong in the direction of strong magnetic fields along large mass agglomerations such as the supergalactic plane [3], a deflection of several degrees at the most is expected along most other lines of sight for nucleons above  $10^{20}$  eV, due to the Faraday rotation limit on the large-scale field. For next generation experiments with their anticipated much improved exposure, this opens up the possibility to do “particle astronomy” and pinpoint sources along the arrival directions.

It has been noted in that respect that a sub class of events above  $4 \times 10^{19}$  eV seems to cluster in arrival directions [4]. If these clusters originated in discrete sources, some interesting qualitative consequences result already, such as a limit on the intercepted magnetic fields that is comparable to the Faraday rotation limit [5]. Next generation experiments should in this case see clusters of several tens or even hundreds of events at these energies in case of the Pierre Auger Project [6] and the Orbital Wide-angle Light Collector (OWL) [8], respectively. This just follows from scaling to the relevant expected exposures. A data pool of arrival directions, times, and energies of that size contains a substantial amount of information on both the source of a given cluster of events and magnetic fields intercepting the line of sight.

This motivated us to conduct a detailed feasibility study for the potential of future experiments to reconstruct certain parameters that characterize the source mechanism and the large-scale magnetic field both of which are poorly known at present. We first briefly describe our method and then summarize our results and give some examples.

## DESCRIPTION OF APPROACH

Here we describe the essential ingredients of our numerical approach; more details can be found in Refs. [9,10].

The propagation of nucleons through extragalactic space is simulated using the Monte Carlo technique: First, a magnetic field realization is set up on a grid via Fast Fourier Transformation by sampling a power spectrum of the form  $\langle B^2(k) \rangle \propto k^{n_B}$  for wavenumbers  $k < 2\pi/l_c$  and 0 otherwise, where  $l_c$  characterizes the coherence scale and  $n_B$  the magnetic field power spectrum. As results are quite insensitive to  $n_B$ , we assume  $n_B = 0$  if not stated otherwise. More sophisticated models for the magnetic field including the role of the large scale structure of galaxies, for example, along the lines discussed in Ref. [3], may be implemented in the future. Many nucleon trajectories are then calculated between a given source and observer by sampling direction of emission, injection energy and the stochastic pion production loss that becomes important above the Greisen-Zatsepin-Kuzmin (GZK) cut-off [11] at a few  $10^{19}$  eV. Pair production by protons has been incorporated as a continuous energy loss. One of the main problems that has to be solved when images of discrete sources are discussed, has not been considered in other work on propagation and deflection [12] and consists of the fact that different trajectories not only originate at the same source, but also have to reach the same observer.

From the injection energies, direction, time, and energy of arrival recorded for the trajectories we then calculate histograms for the distribution in these quantities by convolving with the injection spectrum (typically a power law with index  $\gamma$  for the differential spectrum) in energy and with a timescale  $T_S$  that characterizes the emission timescale. Histograms are also smeared out in energy to account for finite energy resolution (typically  $\Delta E/E \simeq 0.14$ , a value expected for future detectors) and are proportional to the source fluence  $N_0$ . We also use the parameter

$$\tau_E \simeq 2.0 \left( \frac{D}{30 \text{ Mpc}} \right)^2 \left( \frac{E}{100 \text{ EeV}} \right)^{-2} \left( \frac{B_{\text{rms}}}{10^{-11} \text{ G}} \right)^2 \left( \frac{l_c}{1 \text{ Mpc}} \right) \text{ yr.} \quad (1)$$

which is the average time delay for a proton of energy  $E$  over a distance  $D$  in a field of r.m.s. strength  $B_{\text{rms}}$  when energy loss is negligible, and  $\tau_E \ll D$  [13]. It is related to the average deflection angle  $\theta_E$  by

$$\theta_E \simeq 0.02^\circ \left( \frac{D}{10 \text{ Mpc}} \right)^{-1/2} \left( \frac{\tau_E}{1 \text{ yr}} \right)^{1/2}. \quad (2)$$

The subscript  $E$  is given in EeV in the following.

Clusters of events are then obtained by sampling the histogram with Poisson statistics over a time window of width  $T_{\text{obs}}$  which constitutes the experimental lifetime, at a random position. Conversely, for a given cluster of events, a likelihood can be calculated for a given histogram that corresponds to certain values of the physical parameters described above. Averaging over different observational window positions and different realizations of the magnetic field for the same parameters yields the likelihood function  $\mathcal{L}(\tau_{100}, T_S, D, \gamma, N_0, l_c, n_B)$ . Marginalization over part of these parameters, using priors that account for certain constraints and other available information, can be used to reduce the parameter space.

## RESULTS AND EXAMPLES

We first give a brief outline of the main features of the angle-time-energy images of clusters of ultra-high energy nucleons which have been described in detail in Ref. [14].

If both  $T_S < \tau_{100}$ , and  $\tau_{100}$  is small compared to  $T_{\text{obs}}$ , arrival time and energy are correlated according to  $\tau_E \propto E^{-2}$ ; see Eq. (1). The angular image can not be resolved in this case.

A source, such that  $\tau_{100} \gg T_S$  and  $\tau_{100} \gg T_{\text{obs}}$ , can be seen only in a limited range of energies, at a given time, as first pointed out in Ref. [13], and demonstrated in Fig. 1. Below the GZK cut-off, the width of this stripe, in the time-energy plane and within the observational window of length  $T_{\text{obs}}$ , is then governed by the ratio  $D\theta_E/l_c$  for the energy at which events are observed: If this ratio is much smaller than 1, all nucleons have experienced the same magnetic field structure during their propagation and the width is very small in the absence of pion production; in the opposite case the width is expected to be  $\Delta\tau_E/\tau_E \sim 60\%$ , even for negligible energy loss. Furthermore, the angular image is point-like or diffuse, with  $\theta_E$  describing the systematic off-set from the direction to the source, or the angular extent of the diffuse image that is centered on the source, respectively, in these two cases. If  $D\theta_E/l_c \sim 1$ , several images of the source can result [15].

For a source emitting continuously at all energies of interest here, *i.e.* with  $T_S \gg \tau_{30}$  and  $T_S \gg T_{\text{obs}}$ , events of any energy can be recorded at any time. Whereas the above remarks on the angular image now apply for all energies (see Fig. 2), the distribution of arrival time *vs.* energy is now uniform.

Finally, for a source, such that  $\tau_{100} < T_S$  and  $\tau_{30} > T_S$ , together with  $T_S \gg T_{\text{obs}}$ , there exists an energy  $E_C$ , such that  $\tau_{E_C} = T_S$ . In this case, protons with  $E < E_C$  are not detected, as they could not have reached us within  $T_{\text{obs}}$ . However, protons with  $E > E_C$  are detected as for a continuously emitting source, *i.e.* with a uniform distribution of arrival times *vs.* energy (see, e.g., Fig. 3).

We now summarize results on the potential to reconstruct the parameters  $\tau_{100}$ ,  $T_S$ ,  $D$ ,  $\gamma$ ,  $N_0$ ,  $l_c$ , and  $n_B$  in these scenarios. Details have been presented in Ref. [10].

The likelihood presents different degeneracies between different parameters, which complicates the analysis. As an example, the likelihood is degenerate in the ratios  $N_0/T_S$ , or  $N_0/\Delta\tau_{100}$ , with  $N_0$  the total fluence, and  $\Delta\tau_{100}$  the spread in arrival time: these ratios represent rates of detection. Another example is given by the degeneracy between the distance  $D$  and the injection energy spectrum index  $\gamma$ . Yet another is the ratio  $D\theta_E/l_c \propto (D\tau_E)^{1/2}/l_c$ , that controls the size of the scatter around the mean of the  $\tau_E - E$  correlation. Therefore, in most general cases, values for the different parameters cannot be pinned down, and generally, only domains of validity are found. We remark, however, that the generic scenarios discussed above are, in general, easy to distinguish from the likelihood function (see, e.g., Fig. 2).

We find that the distance to the source is obtained from the pion production signature, above the GZK cut-off, when the emission timescale of the source dominates over the time delay. The lower the minimal energy above which the source appears as emitting continuously, the higher the accuracy on the distance  $D$ . The error on  $D$  is, in the best case, typically a factor 2, for one cluster of  $\simeq 40$  events. In this case, where the emission timescale dominates over the time delay at all observable energies, information on the magnetic field is only contained in the angular image. Qualitatively, the size of the angular image is proportional to  $B_{\text{rms}}(Dl_c)^{1/2}/E$ , whereas the structure of the image, *i.e.* the number of separate images, is controlled by the ratio  $D\theta_E/l_c \propto D^{3/2}B_{\text{rms}}/El_c^{1/2}$ . Finally, the case where the time delay dominates over the emission timescale, with a time delay shorter than the lifetime of the experiment, also allows to estimate the distance with a reasonable accuracy.

The injection spectrum index  $\gamma$  can be measured provided ultra-high energy cosmic rays are recorded over a bandpass in energy that is sufficiently broad. In general, it is comparably easy to rule out a hard injection spectrum if the actual  $\gamma \gtrsim 2.0$ , but it is much harder to distinguish between  $\gamma = 2.0$  and 2.5.

The strength of the magnetic field can only be obtained from the time-energy image in this latter case because the angular image will not be resolvable. When the time delay dominates over the emission timescale, and is, at the same time, larger than the lifetime  $T_{\text{obs}}$  of the experiment, only a lower limit corresponding to  $T_{\text{obs}}$ , can be placed on the time delay, hence on the strength of the magnetic field. When combined with the Faraday rotation upper limit, this would nonetheless allow to bracket the r.m.s. magnetic field strength within a few orders of magnitude. Here as well, significant information is contained in the angular image.

The coherence length enters the ratio  $(D\tau_E)^{1/2}/l_c$  that controls the scatter around the mean of the  $\tau_E - E$  correlation in the time-energy image. It can therefore be estimated from the width of this image, provided the emission timescale is dominated by  $\tau_E$  (otherwise the correlation would not be seen), and some prior information on  $D$  and  $\tau_E$  is available. If the source appears continuous and the time delay is large enough to resolve the angular image,  $l_c$  can be constrained or even estimated from the fact that  $D\theta_E/l_c$  passes through 1 at the energy where the scatter  $\Delta\theta_E/\theta_E$  becomes comparable to 1 (it is much smaller at energies that are higher but still below the GZK cut-off; see Fig. 2). Our simulations showed no

sensitivity to the magnetic field power spectrum characterized by  $n_B$ .

An emission timescale much larger than the experimental lifetime may be estimated if a lower cut-off in the spectrum is observable at an energy  $E_C$ , indicating that  $T_S \simeq \tau_{E_C}$ . The latter may, in turn, be estimated from the angular image size via Eq. (2), where the distance can be estimated from the spectrum visible above the GZK cut-off, as discussed above. An example for this scenario is shown in Fig. 3. For angular resolutions  $\Delta\theta$ , timescales in the range

$$3 \times 10^3 \left( \frac{\Delta\theta}{1^\circ} \right)^2 \left( \frac{D}{10 \text{ Mpc}} \right) \text{ yr} \lesssim T_S \simeq \tau_E \lesssim 10^4 \dots 10^7 \left( \frac{E}{100 \text{ EeV}} \right)^{-2} \text{ yr} \quad (3)$$

could be probed. The lower limit follows from the requirement that it should be possible to estimate  $\tau_E$  from  $\theta_E$ , using Eq. (2), otherwise only an upper limit on  $T_S$ , corresponding to this same number, would apply. The upper bound in Eq. (3) comes from constraints on maximal time delays in cosmic magnetic fields, such as the Faraday rotation limit in case of the cosmological large-scale field (smaller number) and knowledge on stronger fields associated with the large-scale galaxy structure (larger number). Eq. (3) constitutes an interesting range of emission timescales for many conceivable scenarios of ultra-high energy cosmic rays. For example, the hot spots in certain powerful radio galaxies that have been suggested as ultra-high energy cosmic ray sources [16], have a size of only several kpc and could have an episodic activity on timescales of  $\sim 10^6$  yr.

## CONCLUSIONS

A wealth of information on both the production mechanism of highest energy cosmic rays and on the structure of large-scale magnetic fields is encoded in angle-time-energy images of discrete sources. If the clustering suggested by AGASA is real, tens (for the Pierre Auger Project) to hundreds (for the OWL Project) of events above a few  $10^{19}$  eV can be expected from individual sources alone. With resolutions of 10-20% in energy and fractions of a degree in angle, next generation experiments should be able to exploit this information.

Special thanks go to Martin Lemoine for an ongoing extensive collaboration on this subject. I also thank Angela Olinto and David Schramm for collaboration in earlier stages. This work was supported, in part, by the DoE, NSF, and NASA at the University of Chicago.

## REFERENCES

1. G. Sigl, D. N. Schramm, and P. Bhattacharjee, *Astropart. Phys.* **2**, 401 (1994).
2. J. W. Elbert, and P. Sommers, *Astrophys. J.* **441**, 151 (1995).
3. for a discussion of this case see, e.g., P. L. Biermann, H. Kang, J. P. Rachen, and D. Ryu, e-print astro-ph/9709252, to appear in Proc. Moriond Meeting on High Energy Phenomena, Jan. 1997, Les Arcs.

4. N. Hayashida et al., *Phys. Rev. Lett.* **77**, 1000 (1996).
5. G. Sigl, D. N. Schramm, S. Lee, and C. T. Hill, *Proc. Natl. Acad. Sci. USA* **94**, 10501 (1997).
6. J. W. Cronin, *Nucl. Phys. B (Proc. Suppl.)* **28B**, 213 (1992); The Pierre Auger Observatory Design Report (2nd ed.) 14 March 1997.
7. Proc. of *International Symposium on Extremely High Energy Cosmic Rays: Astrophysics and Future Observatories* (Institute for Cosmic Ray Research, Tokyo, 1996).
8. J. F. Ormes et al., in *Proc. 25th International Cosmic Ray Conference* (Durban, 1997), eds.: M. S. Potgieter et al., 5, 273; Y. Takahashi et al., in [7], p. 310.
9. G. Sigl, M. Lemoine, and A.V. Olinto, *Phys. Rev. D* **56**, 4470 (1997).
10. G. Sigl and M. Lemoine, e-print astro-ph/9711060, submitted to *Astropart. Phys.*
11. K. Greisen, *Phys. Rev. Lett.* **16**, 748 (1966); G. T. Zatsepin and V. A. Kuzmin, *Pis'ma Zh. Eksp. Teor. Fiz.* **4**, 114 (1966) [*JETP. Lett.* **4**, 78 (1966)].
12. see, e.g., G. A. Medina Tanco, E. M. de Gouveia Dal Pino, and J. E. Horvath, *Astropart. Phys.* **6**, 337 (1997); R. Lampard, R. W. Clay, and B. R. Dawson, *Astropart. Phys.* **7**, 213 (1997).
13. E. Waxman and J. Miralda-Escudé, *Astrophys. J.* **472**, L89 (1996).
14. M. Lemoine, G. Sigl, A. V. Olinto, and D.N. Schramm, *Astrophys. J.* **486**, L115 (1997).
15. M. Lemoine and G. Sigl, work in progress.
16. J. P. Rachen, and P. L. Biermann, *Astron. Astrophys.* **272**, 161 (1993).

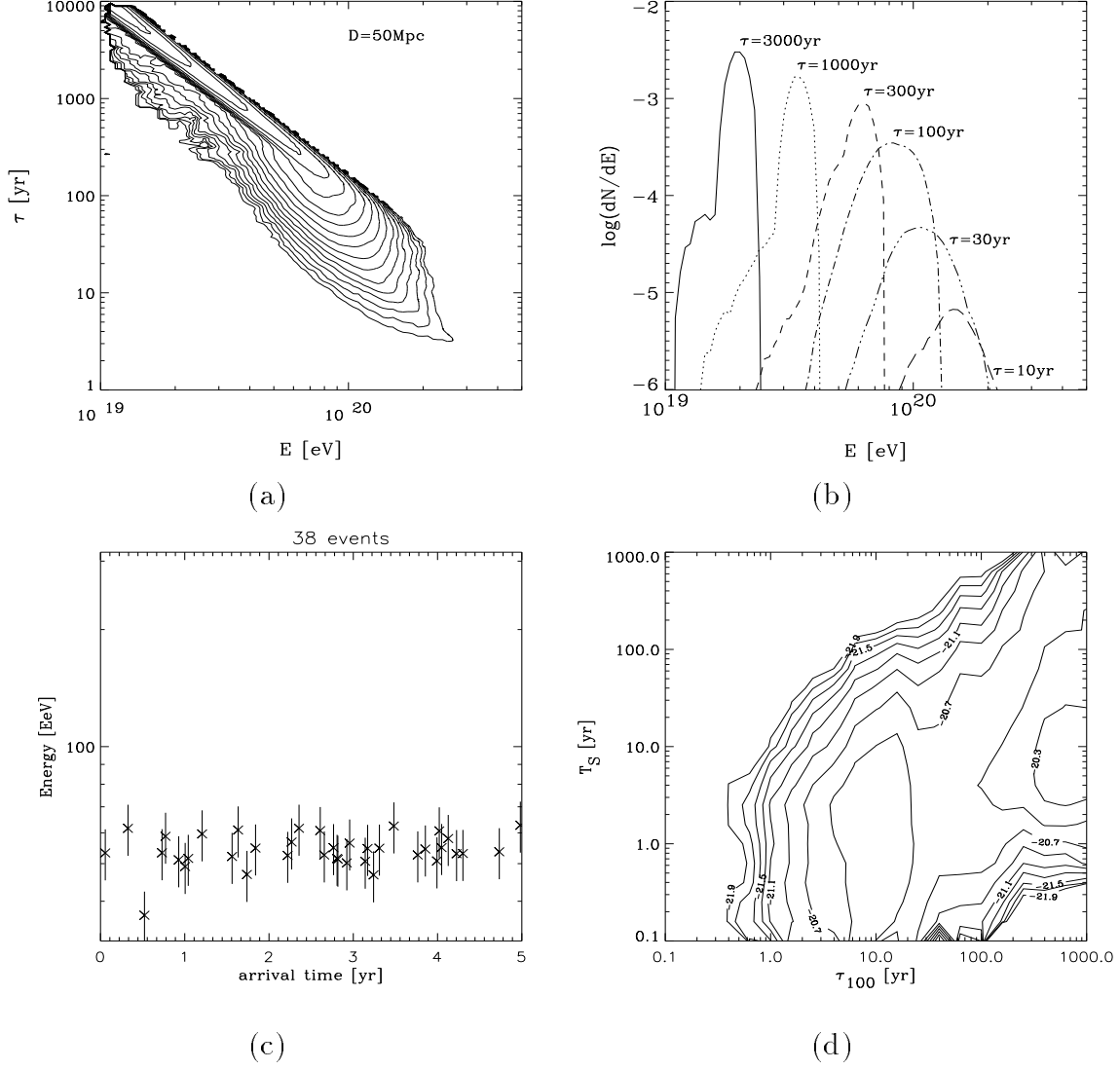


**FIGURE 1.** (a) An arrival time-energy histogram for  $\gamma = 2.0$ ,  $\tau_{100} = 100$  yr,  $T_S \ll \tau_{100}$ ,  $l_c \simeq 1$  Mpc,  $D = 50$  Mpc, corresponding to  $B_{\text{rms}} \simeq 4 \times 10^{-11}$  G. Contours are in steps of a factor  $10^{0.4} = 2.51$ ; (b) Observable energy spectrum for several positions of the observational window in the histogram in (a); (c) Example for a cluster in the arrival time-energy plane resulting from one of the cuts shown in (b); (d) The likelihood function, marginalized over  $N_0$  and  $\gamma$ , for  $D = 50$  Mpc,  $l_c = 0.25$  Mpc, for the cluster shown in (c), in the  $T_S - \tau_{100}$  plane. The contours shown go from the maximum down to about 0.01 of the maximum in steps of a factor  $10^{0.2} = 1.58$ . The fall-off at  $\tau_{100} \gtrsim 50$  yr and  $T_S \lesssim 3$  yr is a numerical artifact due to limited statistics. The true parameters are reasonably well reconstructed.

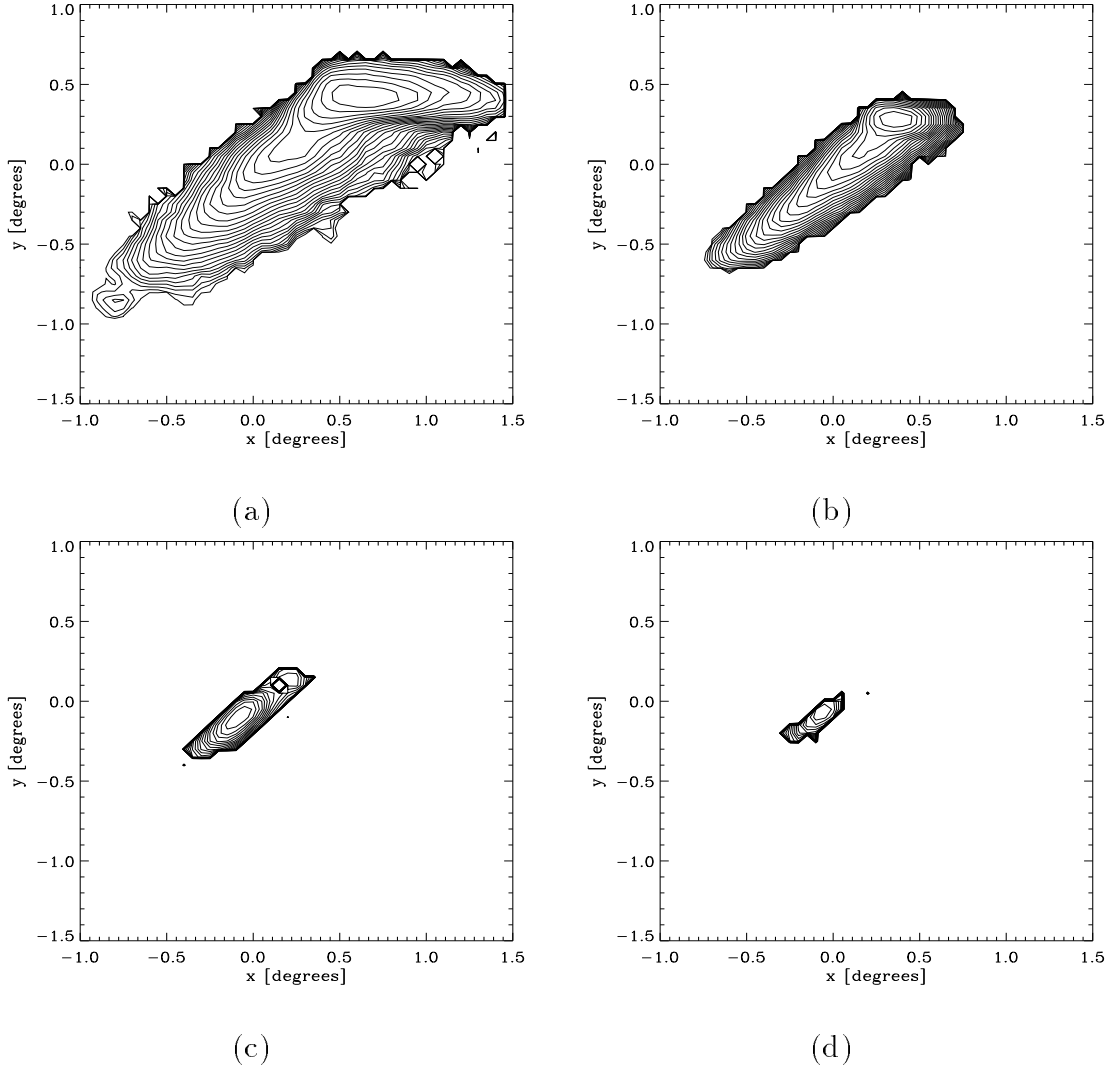


**FIGURE 2.** An angle-histogram for  $\gamma = 2.0$ ,  $\tau_{100} = 10^4$  yr,  $T_S \gg \tau_{100}$ ,  $l_c \simeq 1$  Mpc,  $D = 50$  Mpc, corresponding to  $B_{\text{rms}} \simeq 4 \times 10^{-10}$  G. An angular resolution of  $0.05^\circ$  was assumed. The point  $x = y = 0$  is the source position and the contours decrease in steps of 0.1 in the logarithm to base 10. (a) Image integrated over all energies  $E > 30$  EeV. Two partially blended, elongated images at  $x \simeq 0.2^\circ$ ,  $y \simeq 0.2^\circ$  and at  $x \simeq 0.7^\circ$ ,  $y \simeq 0.4^\circ$  are clearly visible, the second one being more luminous by about a factor 4; (b) Same for  $E > 100$  EeV. The two images are now closer to the source position; (c) Same for  $E > 200$  EeV. The second image has almost disappeared; (d) Same for  $E > 300$  EeV. As a consequence,  $D\theta_E/l_c \simeq 1$  for  $E \simeq 100$  EeV. If  $D$  can be estimated from the energy spectrum, an estimate for  $l_c$  results.



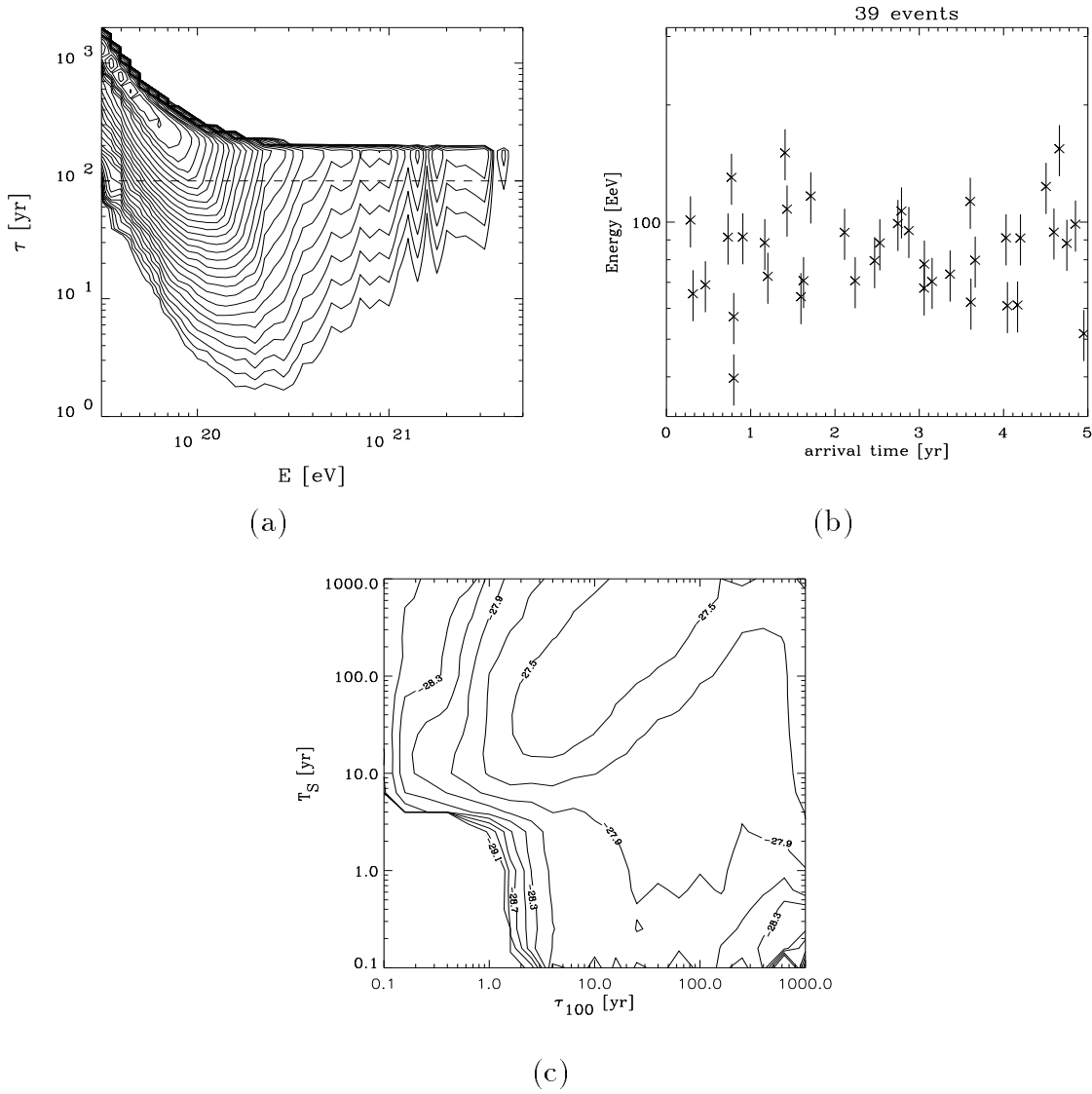


**FIGURE 3.** (a) An arrival time-energy histogram for  $\gamma = 2.0$ ,  $\tau_{100} = 50$  yr,  $T_S = 200$  yr,  $l_c \simeq 1$  Mpc,  $D = 50$  Mpc, corresponding to  $B_{\text{rms}} \simeq 3 \times 10^{-11}$  G. Contours are in steps of a factor  $10^{0.4} = 2.51$ ; (b) Example for a cluster in the arrival time-energy plane resulting from the cut indicated in (a) by the dashed line at  $\tau \simeq 100$  yr; (c) Same as Fig. 1 (d), but for the cluster shown in (b). Note that the likelihood clearly favors  $T_S \simeq \tau_{50}$ . For  $\tau_{100}$  large enough to be estimated from the angular image size,  $T_S \gg T_{\text{obs}}$  can, therefore, be estimated as well.